Effect of Direct Aging on Heat-Affected Zone and Tensile Properties of Electrospark-Deposited Alloy 718

PABLO D. ENRIQUE, ZHEN JIAO, and NORMAN Y. ZHOU

The degradation of high-temperature components in the aerospace industry becomes a greater concern with the use of higher operating temperatures and increased operating cycles. Although the repair of defects can extend component lifespans, welding often results in a heat-affected zone (HAZ) or fusion zone with reduced mechanical properties. Due to the low energy input of electrospark deposition (ESD), repaired components should be less susceptible to mechanical property deterioration. ESD of alloy 718 on solution-annealed and aged alloy 718 base metal is evaluated in the as-deposited and direct-aged condition. HAZ formation is measured at 80 μm on an annealed substrate and 40 μm on an aged substrate. Direct aging of depositions eliminates the heat-affected zone and introduces strengthening phases in the deposition that results in a hardness equivalent to that of the aged base metal. The yield strength of as-deposited and direct-aged alloy 718 depositions is equivalent to the annealed and aged base metal, respectively, whereas the ultimate strength is, respectively, 16 and 8 pct lower. Decreased ultimate strength is attributed to lower fracture toughness of brittle secondary phases and splat boundaries from the ESD process that remain after the direct aging heat treatment.

https://doi.org/10.1007/s11661-018-4997-1

I. INTRODUCTION

COMPONENT lifespan is a significant point of interest in the aerospace industry,[1,2] including airplane turbine engine parts and more so with the recent trend by SpaceX towards fully reusable space-fairing vehicles. An incentive to operate at higher temperatures is driven by improved engine efficiencies, and is made possible by advances in cooling efficiency.[3] The result is higher thermal stresses, leading to lower component lifespans. Certain components—such as airplane turbine blades—also experience significant centrifugal loading, aerodynamic forces, and airflow instability/perturbations.[2] These effects contribute to thermally and mechanically induced failure, caused by crack growth originating from internal, surface, or coating defects.

Alloy 718 is a Ni-superalloy widely used in components capable of withstanding high temperatures and corrosive environments. In addition to retaining their high strength and creep deformation resistance at high temperatures, alloy 718 also exhibits good oxidation resistance due to the presence of alloying elements that form passivating surface oxide layers for temperatures up to 900 °C.[4] This Ni-superalloy is commonly used in the aerospace industry. Applications include structural and rotating components in airplane turbine engines[5,6] and space vehicle components like the space shuttle main engine, which contained over 50 pct alloy 718 by weight.[7]

Material and manufacturing costs make alloy 718 component repair an attractive option, avoiding the need to scrap parts when defects are detected. However, most welding repair processes introduce considerable heat-affected zones that weaken the base metal and reduce the component's flight reliability. Electrospark deposition (ESD) is a micro-welding process that uses short duration electrical pulses to deposit electrode materials onto conductive substrates. The small energy input and high cooling rate associated with ESD is expected to result in minimal damage to the base metal, making this repair technique ideal for critical components. The study presented here quantifies the ESD-induced heat-affected zone (HAZ) formation in solution-annealed and aged alloy 718 substrates, showing that HAZ sizes are 80 and 40 μm, respectively. A direct aging heat treatment is found to eliminate the presence of the heat-affected zone when evaluated using microhardness measurements in both annealed and aged substrates. The strength of deposited alloy 718 compares

PABLO D. ENRIQUE and NORMAN Y. ZHOU are with the University of Waterloo, 200 University Avenue W, Waterloo, ON N2L 3G1, Canada. Contact e-mail: pdenriqu@uwaterloo.ca ZHEN JIAO is with Huys Industries Ltd., 175 Toryork Drive, Unit 35, Weston, ON M9L 1X9, Canada.

Manuscript submitted July 2, 2018.
Article published online November 2, 2018

favorably with the annealed substrate in the as-deposited state and compares favorably with the aged substrate after the direct aging heat treatment.

II. EXPERIMENTAL METHODS

A. *Materials and Processes*

The EDX measured alloy 718 base metal and electrode composition is given in Table I, with the base metal received in the annealed condition (980 °C for 1 hour).

The ESD process works by transferring droplets of material from a consumable electrode onto a substrate.[8,9] The quantity of material transferred is a function of the energy input, which is based on voltage and capacitance parameters (90 V, 120 μF). The frequency of capacitor discharge (which controls the frequency of droplet transfer) is controlled by setting a frequency parameter (170 Hz). ESD was performed with the use of a commercial Huys Industries machine. Ultrapure argon cover gas was applied coaxially around the electrode at a flow rate of 10 L min^{-1} during depositions. Samples for microhardness testing were prepared by coating a 0.7-mm-thick base metal substrate with 10 layers of deposited alloy 718. Each layer was applied using a raster scan pattern along a square 7 mm by 7 mm area, and a hand-held motorized peening tool was used after each layer was deposited to reduce surface roughness. Peening is performed by placing into contact a vibrating hardened tool steel pin on the surface of the deposition and moving in a raster scan pattern for 20 s per layer. The work imparted on the surface is controlled through the use of a 0.04-mm offset counter weight.

Double U-joint repaired samples for tensile testing were prepared by creating a 5 mm by 7 mm cavity with a depth of 0.4 mm in the center of the top surface of a tensile testing specimen, filling the cavity, and then repeating the process on the opposite side of the tensile specimen (Figure 1(a)). Peening was performed at 5 min intervals during the repair of the tensile specimens, which on average required 57 min of repair time.

An aging heat treatment was performed on base metal and repaired samples in an inert high purity argon environment at a flow rate of 3 mL min^{-1}. Samples to be aged were placed in a ceramic crucible, loaded into a furnace at room temperature, heated at 5 °C min^{-1} to 720 °C, held at 720 °C for 8 hours, furnace cooled to 620 °C, and held for 10 hours, after which the samples were removed and air cooled.

Table I. EDX Measurements (Weight Percent) for Alloy 718 Base Metal and Electrode

Alloy 718	Ni	Cr	Nb	Mo	Ti	Al	Si	Fe
Base Metal	54.0	19.7	3.3	2.6	1.1	0.3	—	19.0
Electrode	53.7	19.2	3.8	2.8	1.0	0.3	0.2	19.0

B. *Characterization and Testing*

Schematics of the double-notched, double U-joint repaired tensile testing specimens are shown in Figure 1, with the repair of the specimen performed as described in Section II–A. The 1-mm-wide, 3-mm-long notches that form the neck of the tensile specimen were prepared after the double U-joint repair with the use of a Struers Accutom-50 precision saw. The neck of repaired specimens is composed solely of deposited material to determine the yield and ultimate strength without influence of the base metal. Two-tailed t-tests are performed to compare the mean yield and ultimate strength values of repaired and base metal specimens, with a confidence level of 95 pct ($p < 0.05$) indicating a statistically significant result. An adjusted Hedge's g value for small sample sizes (total number of samples = 25) is used to determine whether the result is meaningful in magnitude ($g > 0.8$ indicates a large difference).

Microstructure evaluation was performed using an Oxford BX51M optical microscope (OM) and a Zeiss UltraPlus field emission scanning electron microscope (FE-SEM) with EDX mapping and BSE capabilities. Fractography evaluation was performed using a JEOL JSM-6460 SEM with EDX capabilities. All SEM images were acquired at an accelerating voltage of 20 kV and 60 μm aperture. Microhardness measurements were performed on a Wolpert Wilson 402 MVD micro Vickers hardness tester (100 gf and 15 s dwell time) and tensile testing is done on an Instron 5548 micro tensile tester at 1 mm min^{-1} extension speed. An inverted glyceregia etchant (HCl:HNO_3:Glycerol in a 5:1:1 ratio) is used for etching of the alloy 718 samples, with an etching time of 10 s to 2 min depending on the features being investigated.

III. RESULTS AND DISCUSSION

A. *Microstructure*

As-received solution-annealed alloy 718 exhibits an equiaxed austenitic γ matrix as shown in Figure 2(a) with some twinning and undissolved carbide phases that were not fully solutionized by the annealing process. As-deposited alloy 718 exhibits elongated grains that traverse splat boundaries in the build-up direction, shown in Figure 2(b). The deposited material exhibits an average grain size of 7.4 ± 1.5 μm perpendicular to the growth direction, compared to the larger substrate grain size of 12.6 ± 2.2 μm. These measurements were made using the intercept method and confirmed using threshold analysis, without the use of stereological corrections. These measurements are comparable to grain sizes reported in literature for ESD-processed and base metal alloy 718.[10] The cellular dendritic solidification microstructure of the as-deposited material is shown in Figure 2((c), (d)) with primary dendrite spacing of approximately 1 μm. Backscattered electron (BSE) imaging of the deposition (Figure 2(d)) indicates that the segregation of heavier elements occurs in the interdendritic regions.

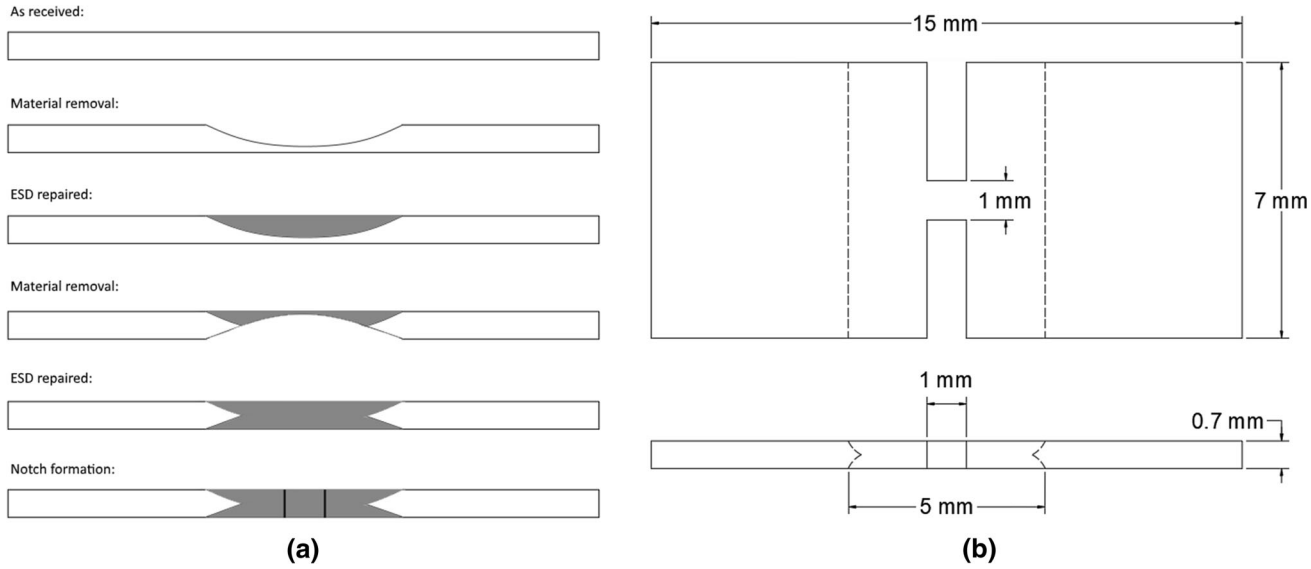

Fig. 1—Schematic of (*a*) tensile specimen fabrication process with the double U-joint repair and (*b*) specimen dimensions.

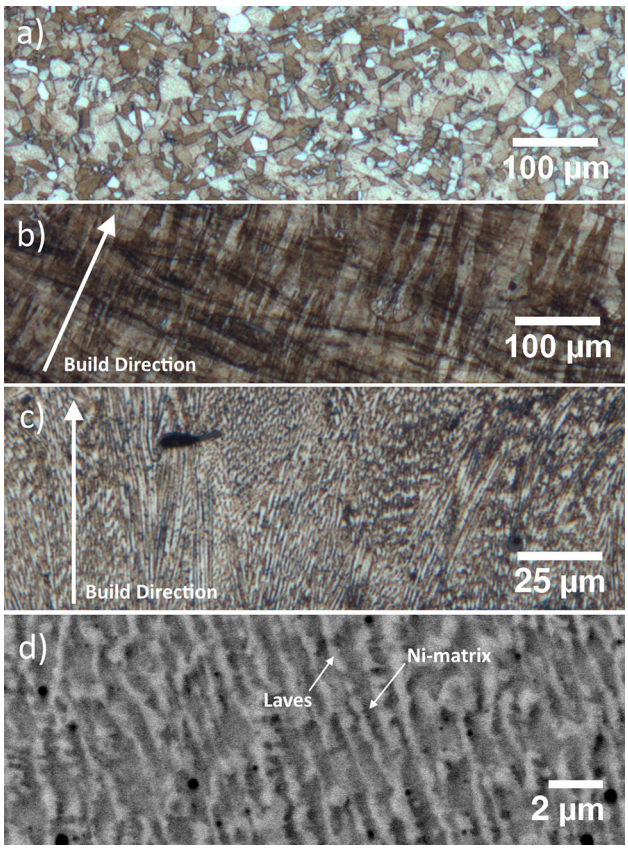

Fig. 2—OM images of etched (*a*) equiaxed substrate grains, (*b*) elongated deposition grains, (*c*) cellular dendritic subgrain within deposition, and (*d*) SEM image (BSE) of dendrite (Ni-matrix) and interdendritic (Laves) regions.

This has been reported to consist of a Nb-rich Laves phase common in welded alloy 718 that occurs during solidification.[11–13]

After aging, no significant grain coarsening was observed in the deposition or substrate and the deposition retained its solidification microstructure. Large carbide phases were identified in both the deposition and substrate. Ti-rich carbonitrides and Nb-rich carbide precipitates are shown in Figure 3 and are identified with the use of EDX. Their respective compositions are listed in Table II, and the visual characteristics (Ti-rich carbonitrides appearing orange and Nb-rich carbides appearing beige) match previous studies in literature.[14] Both phases appear in the direct-aged deposited alloy 718 (Figures 3((c), (d)) which suggests that the presence of the interdendritic laves phase shown in the as-deposited (Figure 4(a)) and direct-aged condition (Figure 4(b)) does not completely deplete the Nb available for forming other phases. The size of microstructural features in electrospark-deposited alloy 718 has been shown to vary with process conditions and the thickness of deposited material,[15] resulting in regions with thicker and thinner interdendritic Laves regions. However, the quantity of Laves phase remains constant between the as-deposited and direct-aged deposition, suggesting that Nb within the Laves phase does not solutionize into the matrix or contribute to other Nb-rich phases (carbides, γ'', δ) after a direct aging heat treatment.

Also detected in the substrate and deposited alloy 718 in the aged condition were carbides with aluminum and magnesium additions. Literature studies of nickel superalloys with trace quantities of Mg have reported Mg segregation along the grain boundaries[16] and into carbide phases.[17] A more in-depth look shows that these carbides are non-uniform, with a core rich in Mg, Al, and O, and a shell region rich in Ti and Nb (Figures 5((b), (c)). This agrees with recent work on the effect of Mg and Ca additions on carbide morphology.[18] However, it was noted that core-shell carbides within the deposited Alloy 718 have significantly smaller shells, seen when

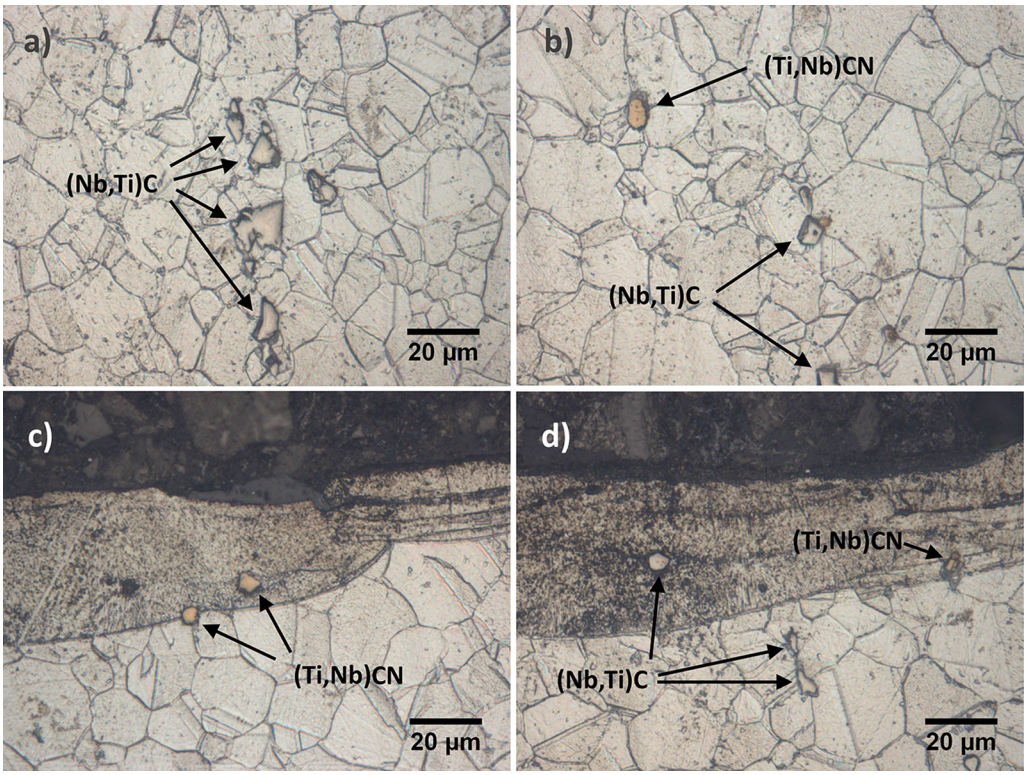

Fig. 3—Etched OM images of Ti-rich and Nb-rich carbides indicated with arrows after (*a–b*) aging of solution-annealed alloy 718 substrate, (*c–d*) direct aging of as-deposited alloy 718.

Table II. Composition (Weight Percent) of Phases Detected with EDX (Excluding Carbon)

	Ti		Nb		N	
Phase	At. Pct	Wt Pct	At. Pct	Wt Pct	At. Pct	Wt Pct
(Nb,Ti)C	12.7	7.0	87.3	93.0		
(Ti,Nb)CN	87.4	89.3	4.1	8.2	8.5	2.5

comparing Figures 5(b) and (c). The microstructure of the region surrounding the carbide may play a role; as shown in Figure 5(c), the Nb-rich Laves phase persists in the deposition even after aging, trapping Nb, and reducing the quantity available to form the (Ti,Nb)CN shell. Poor Nb contrast between the shell and surrounding laves-rich material during EDX mapping in Figure 5(c) supports this hypothesis, since EDX mapping of carbides in a Laves-free region (Figures 5(a) and (b)) shows a Ni-matrix with lower Nb levels.

Trace Mg quantities (on the order of 10 to 100 ppm or 0.001 to 0.01 pct) are not detectable with EDX analysis until segregation occurs. The presence of core-shell carbides in the substrate suggests that the substrate contains Mg below the EDX detection limit. However, the same cannot be said for the alloy 718 electrode. During the ESD process, both the electrode and substrate material experiences localized melting that can introduce Mg into the deposition near the substrate-deposition boundary. Since few core-shell carbides were found in the deposition—and their locations were near the boundary—the presence of Mg in the electrode is unlikely.

A comprehensive review of trace Mg-containing superalloys—including alloy 718—found that Mg did not affect the room temperature tensile strength and fracture properties,[17] although some properties at elevated temperatures—such as ductility and stress rupture life—were affected in some cases. The room temperature, 500 °C, and 650 °C tensile properties of alloy 718 have been shown unaffected by small additions of Mg (up to 100 ppm), and no influence on the general microstructure (grain size or δ-phase quantity and morphology) was found.[19] A similar lack of difference in tensile strength was reported in Mg-containing alloy 718 when core-shell carbides were formed,[18] suggesting that the presence of magnesium in the substrate should not complicate the strength comparisons with the deposition.

The strengthening phase of alloy 718 is primarily γ'' with a Ni_3Nb composition, although a Ni3(Al,Ti) γ' phase

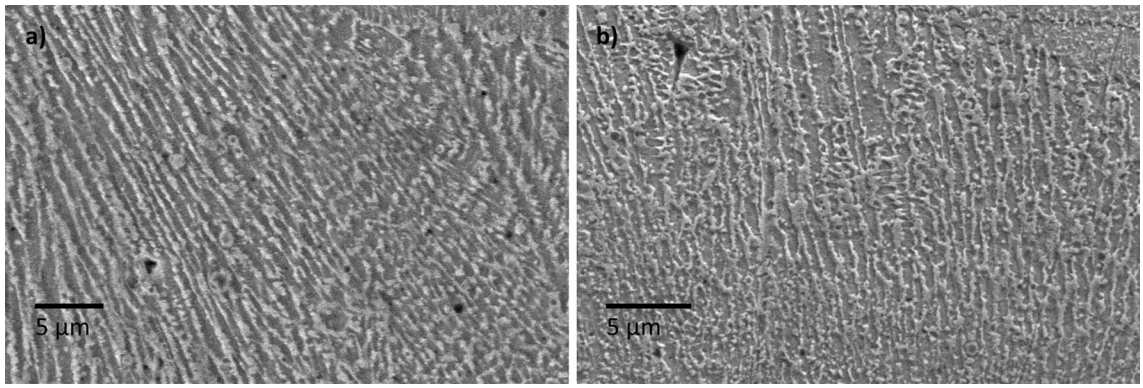

Fig. 4—Etched SEM images of dendritic and interdendritic phases in the (*a*) as-deposited condition and (*b*) direct-aged condition.

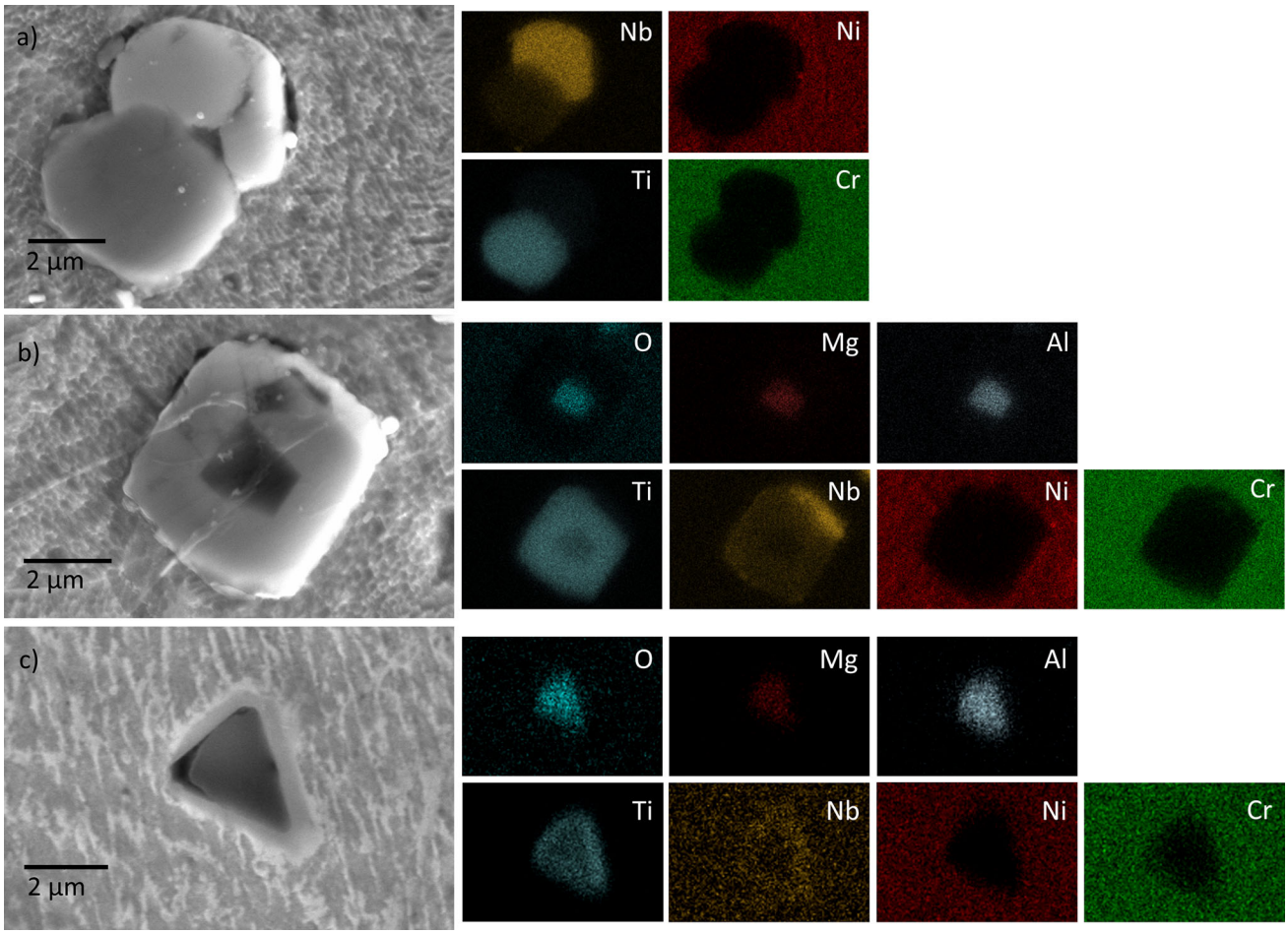

Fig. 5—Etched SEM images of aged substrate alloy 718 with (*a*) adjacent (Nb,Ti)C and (Ti,Nb)CN, (*b*) substrate carbide with (Mg,Al)O core, (Ti,Nb)CN shell, and sliver of (Nb,Ti)C, and (*c*) deposition carbide with (Mg,Al)O core and (Ti,Nb)CN shell.

is also expected to form. These precipitates are not present in annealed or as-deposited alloy 718, and typical particle sizes are approximately 15 to 100 nm in size depending on the extent of aging. Extended aging times or higher heat treatment temperatures result in larger precipitates that are easier to observe *via* SEM,[20–22] whereas properly aged alloy 718 has γ'' and γ' precipitates that are difficult to properly resolve (Figure 6) even with high-resolution FE-SEM.[10,23] Qualitative analysis suggests that a lower quantity of strengthening phases form in the deposition after direct aging than the base metal or HAZ after aging. The deposition's γ'' and γ' precipitates can be found interspersed between larger secondary precipitates in Figure 6(c).

B. *Heat-Affected Zone Formation*

The hardness profile in Figure 7(a) for as-deposited alloy 718 on a solution-annealed substrate shows the presence of an 80-μm heat-affected zone (HAZ). The higher hardness of the deposition in comparison to the annealed substrate prior to heat treatment can be partly attributed to the smaller grain size and fine dendritic solidification microstructure. Smaller grains and subgrains in the deposition should positively influence hardness, which has been shown to follow a Hall–Petch type relationship.[24] Additionally, interdendritic carbide, oxide, and Laves phases are shown to form in ESD alloy 718,[10] which can contribute to the higher hardness in the as-deposited condition.[25]

The hardness increase in the HAZ is potentially the result of grain boundary carbide phases known to form in the HAZ of alloy 718 welds.[26] These may form as a result of ESD-induced heating and cooling cycles, and are known to result in grain boundary strengthening.[25] Other sources of HAZ hardening may arise from peening and oxygen pickup during deposition. The effect of machine hammer peening on alloy 718 has been investigated in literature, with severe grain deformation resulting in nano-sized grains.[27] This grain deformation was credited for the 50 to 100 HV increase at the surface of the specimen, which decayed with increasing depth into the sample. In as-deposited alloy 718 samples, no grain deformation in the HAZ is observed and repeating the deposition without peening does not noticeably influence the hardness within the deposition or HAZ. The difference is likely in the severity of peening, with the hand-held device used in this study having a minimal surface-localized effect that is also eliminated during subsequent deposition due to material re-melting. Peening was never performed directly on the substrate and is unlikely to explain the observed HAZ hardness increase. However, pickup of interstitial elements such as oxygen during welding may result in some solid solution strengthening,[28] with diffusion of oxygen from the weld metal into the HAZ during the repeated heating and cooling cycles of the ESD process contributing to the hardness increase. Since oxides have been observed in as-deposited alloy 718,[10] and were found in this study in Mg- and Al-containing carbides, oxygen is known to exist in a solutionized form prior to aging.

The use of a post-deposition aging step eliminates the presence of the HAZ and results in an even-matched hardness as shown in Figure 7(b), which agrees with similar post-process heat treatments for other welding techniques in literature.[29, 30]

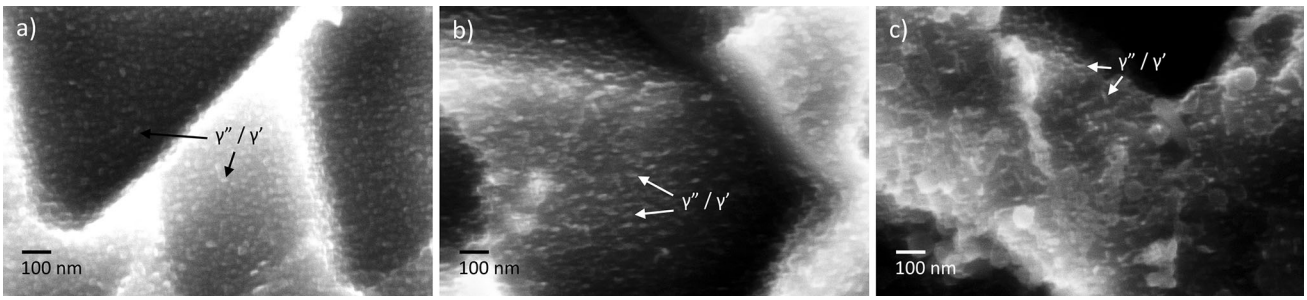

Fig. 6—FE-SEM using the Zeiss InLens SE detector of γ'' and γ' precipitates in an etched (*a*) substrate alloy 718 after aging, (*b*) HAZ after deposition and aging, and (*c*) deposition after direct aging.

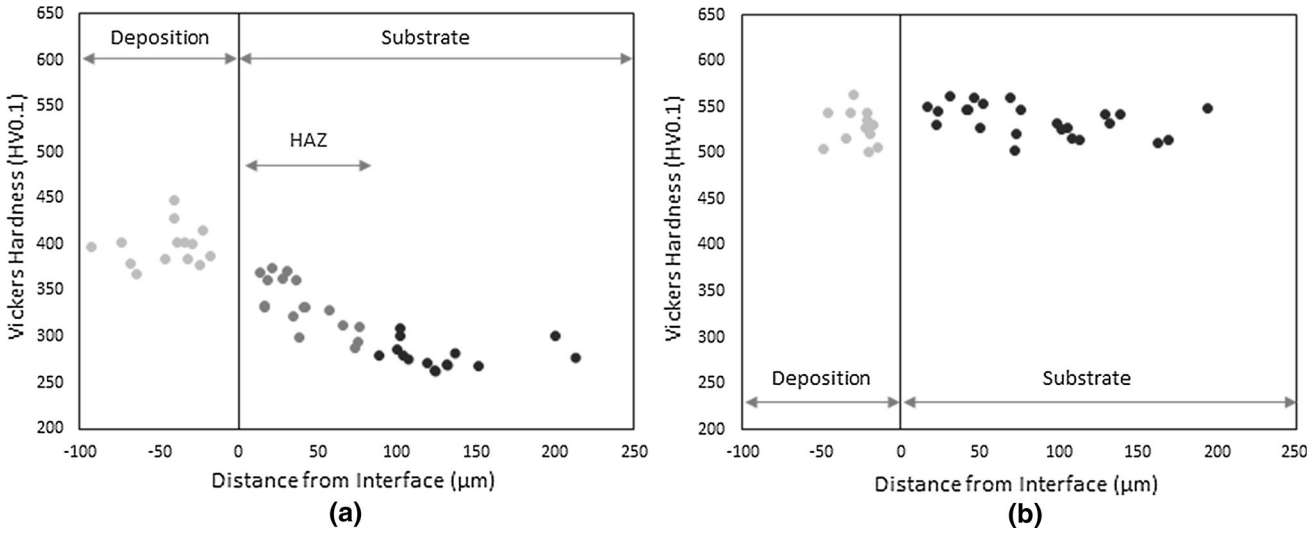

Fig. 7—Alloy 718 depositions on solution-annealed alloy 718 with (*a*) no post-ESD heat treatment and (*b*) with a post-ESD aging treatment.

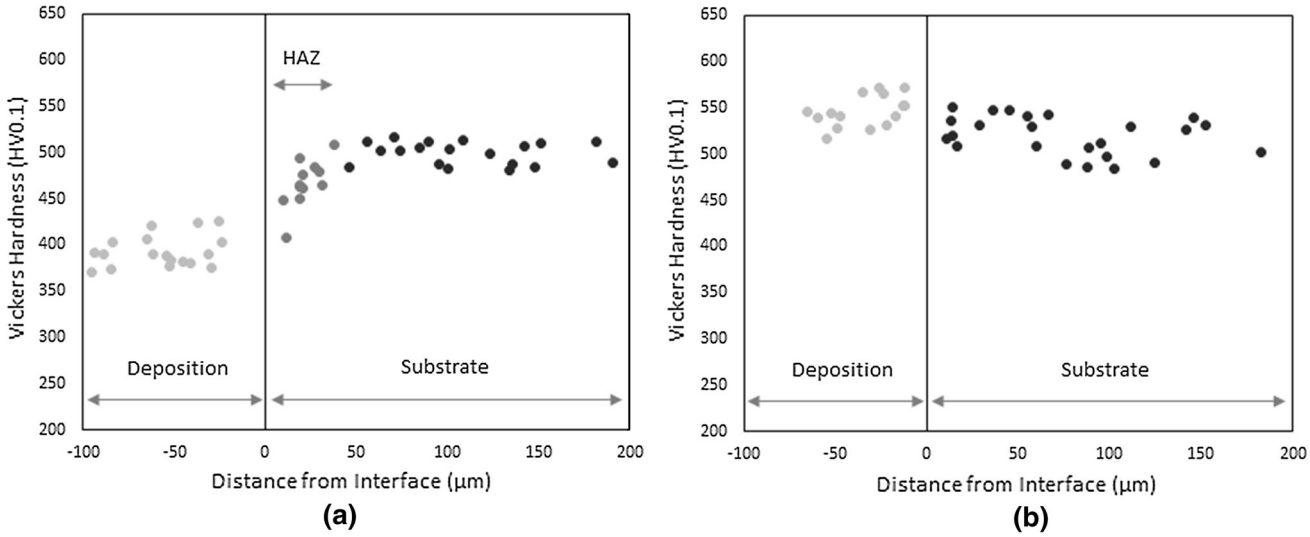

Fig. 8—Alloy 718 depositions on aged alloy 718 with (*a*) no post-ESD heat treatment and (*b*) with a direct aging heat treatment.

Table III. Comparison of HAZ for Alloy 718 Welds by Various Techniques

Welding Technique	Annealed and Aged Substrate
Electrospark Deposition	40 to 80 μm
Electron Beam Welding	300 to 1500 μm[31,32]
Laser Welding	700 to 2500 μm[29,30,33,34]
Gas Tungsten Arc Welding	2000 to 5000 μm[30,35]

The aging process has a non-uniform effect on hardness between the deposition, HAZ, and substrate regions. The extent of aging-induced strengthening in deposited alloy 718 is lower than that of the substrate alloy 718. The Nb-rich Laves phase in the interdendritic regions of as-welded alloy 718 is expected to be detrimental to the formation of the Ni_3Nb γ'' strengthening phase. If annealing is not used to dissolve Nb from the Laves phase back into the γ matrix, the amount of Nb available for the formation of the γ'' phase is reduced. The lack of observable difference in the Laves content between as-deposited and direct-aged alloy 718 depositions indicates that Nb remains trapped within the Laves phase. Reduced availability of Nb was also reflected in the smaller carbides and (Ti,Nb)CN shells within the deposition and the lower strengthening phase quantity. These results closely reflect those of laser-welded solution-treated alloy 718 with direct aging post processing,[29] which demonstrated that the smaller increase in hardness within the weld after direct aging is due to Nb trapped within the Laves phase leading to less strengthening phase formation.

More applicable to the repair of in-service components is the deposition of alloy 718 on an aged alloy 718 substrate. The result is an undermatched deposition hardness, and a 50-pct smaller heat-affected zone of 40 μm (Figure 8(a)) when compared to ESD of alloy 718 on an annealed substrate. This agrees with other studies in literature, where aged alloy 718 is found less sensitive to heat input during welding.[31] Softening of the aged substrate in the HAZ is described in literature as occurring due to precipitate reversion, where heat input from the ESD process solutionizes the strengthening phases back into the nickel matrix.[30] This is supported in Figure 8(b) by the increased hardness of the HAZ after aging and Figure 6(b), where the strengthening phases are reintroduced to the HAZ.

Compared to the welding of alloy 718 using other techniques, ESD results in a significantly smaller HAZ (Table III) due to the lower energy input required to melt and transfer small droplets of material to the substrate.

C. *Tensile Properties and Fracture*

As-deposited and direct-aged depositions of alloy 718 exhibit yield strengths comparable to the solution-annealed and aged base metals, respectively. Direct aging results in a significant yield and ultimate strength increase when compared to the as-deposited condition, as shown in Figure 9, attributed to the formation of the strengthening phase. However, ultimate tensile strength is lower in the as-deposited ($p = 0.011$, $g = 1.65$) and direct-aged conditions ($p = 0.046$, $g = 1.27$) when compared to the solution-annealed and aged base metals, respectively. The design of repaired tensile specimens allow for the strength of the deposition to be tested without HAZ or base metal influence, such that the lower ultimate strength can be attributed directly to the lower fracture toughness of the interdendritic phases and splat boundaries in both the as-deposited and direct-aged conditions.[36]

The matching yield strength but lower ultimate strength when compared to the respective base metal in both the as-deposited and aged condition suggests that plastic deformation is limited in deposited alloy 718. This is made evident by the morphology of the fracture surfaces in Figure 10. The aged substrates exhibit typical ductile fracture and dimpled features,

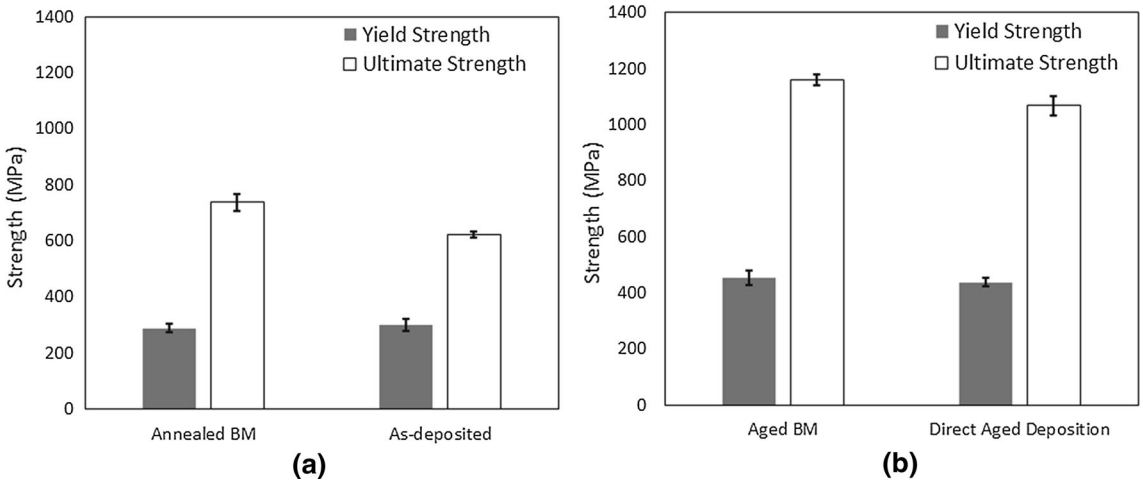

Fig. 9—Tensile test results for (*a*) annealed base metal (BM) and as-deposited alloy 718 with standard error bars and (*b*) after aging heat treatments for BM and deposited alloy 718 with standard error bars.

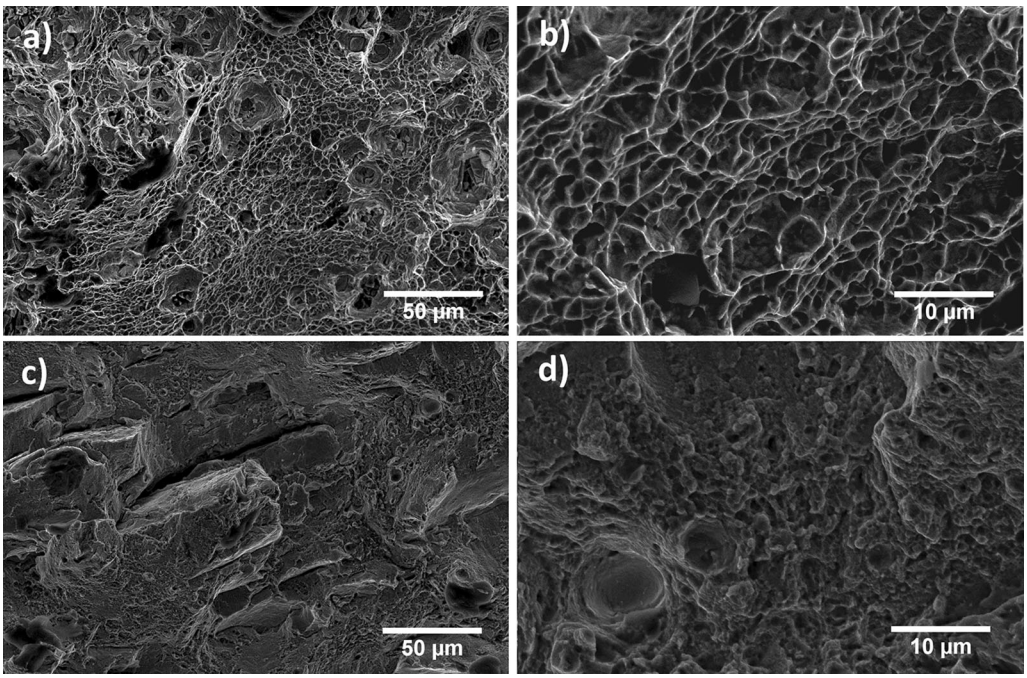

Fig. 10—Fracture surface SEM images of (*a–b*) aged substrate tensile specimen and (*c–d*) direct aged deposition tensile specimen.

which was also seen in annealed substrates.[36] The aged deposition fracture surface contains smaller, shallower dimples, and sharper features that are typical of less ductile fractures,[37] also previously reported for as-deposited alloy 718.[36] EDX was used to identify the phase at the bottom of large dimples along the fracture surface in the aged base metal (Figure 11(a)) and direct-aged deposition (Figure 11(b)) as a (Nb,Ti)C with the composition previously listed in Table II. Cracks can be found within these carbides on the fracture surface, similar to that of direct laser-deposited alloy 718.[33] This has been identified previously in literature as a possible mechanism for crack initiation, occurring not only at the interface between Laves or carbide phases and the γ matrix, but also within these brittle phases.[33]

Closer inspection of the fracture surface in direct-aged samples (Figure 11(c)) shows the presence of dendritic features that can be attributed to the cellular dendritic solidification microstructure in deposited alloy 718. These same features were not present in base metal specimens, suggesting that crack propagation occurs within the brittle intermetallic phases found in the interdendritic regions of deposited alloy 718, and along splat boundaries that form the step-like features shown in Figure 10(c).[36]

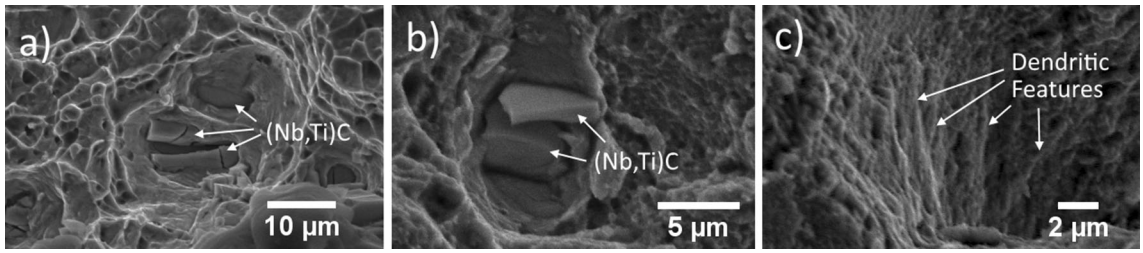

Fig. 11—Fracture surface SEM images of (*a*) (Nb,Ti)C in an aged base metal specimen, (*b*) (Nb,Ti)C in an aged deposition specimen, and (*c*) dendritic features on the fracture surface of an aged deposition specimen.

IV. CONCLUSIONS

1. Heat-affected zone (HAZ) formation in the repair of aged and annealed alloy 718 was measured to be 40 and 80 μm, respectively. The limited HAZ size in comparison to other welding techniques is attributed to lower energy input and greater cooling rates. A direct aging process is found to eliminate the presence of the heat-affected zone when measured using microhardness indentation testing.
2. Hardness recovery non-uniformity is displayed when applying a direct aging heat treatment. A greater increase in hardness is observed in the substrate than the deposition, attributed to the presence of Laves phases in the deposition that limit the availability of Nb to form the γ'' strengthening phase. However, the even-matched hardness between the direct-aged deposition and aged substrate is partly attributed to the fine grain structure and secondary phases in the deposition, which remain after direct aging.
3. The yield strength of as-deposited and direct-aged alloy 718 depositions was statistically similar to that of the annealed and aged base metal, respectively. The ultimate strength of as-deposited and direct-aged alloy 718 depositions was lower than that of the annealed and aged base metal, respectively. This is attributed to lower fracture toughness in splat boundaries and the brittle interdendritic phases that form during ESD and remain in the direct-aged condition. Fracture surface images of the direct-aged deposition indicate that brittle phases may act as crack initiation points, while brittle phases within the interdendritic regions of the deposition may act as crack propagation pathways.

ACKNOWLEDGMENTS

This work was performed with funding support from the Natural Sciences and Engineering Research Council of Canada (NSERC), Huys Industries, and the CWB Welding Foundation, in collaboration with the Centre for Advanced Materials Joining and the Multi-Scale Additive Manufacturing Lab at the University of Waterloo.

REFERENCES

1. D.K. Huzel: *Modern Engineering for Design of Liquid-Propellant Rocket Engines*, American Institute of Aeronautics and Astronautics, 1992.
2. B.A. Cowles: *Int. J. Fract.*, 1996, vol. 80, pp. 147–63.
3. J.H. Perepezko: *Science*, 2009, vol. 326, pp. 1068–69.
4. G.A. Greene and C.C. Finfrock: *Oxid. Met.*, 2001, vol. 55, pp. 505–21.
5. D.F. Paulonis and J.J. Schirra: in *Superalloys 718, 625, 706 and Various Derivatives (2001)*, vol. 718, TMS, 2001, pp. 13–23.
6. R.E. Schafrik, D.D. Ward, and J.R. Groh: in *Superalloys 718, 625, 706 and Various Derivatives (2001)*, TMS, 2001, pp. 1–11.
7. R.P. Jewett and J.A. Halchak: in *Superalloys 718, 625 and Various Derivatives (1991)*, TMS, 1991, pp. 749–60.
8. A. Lešnjak and J. Tušek: *Sci. Technol. Weld. Join.*, 2002, vol. 7, pp. 391–96.
9. J. Liu, R. Wang, and Y. Qian: *Surf. Coat Technol.*, 2005, vol. 200, pp. 2433–37.
10. E. Anisimov, A.K. Khan, and O.A. Ojo: *Mater. Charact.*, 2016, vol. 119, pp. 233–40.
11. L.L. Parimi, G. Ravi, D. Clark, and M.M. Attallah: *Mater. Charact.*, 2014, vol. 89, pp. 102–11.
12. F. Liu, X. Lin, H. Leng, J. Cao, Q. Liu, C. Huang, and W. Huang: *Opt. Laser Technol.*, 2013, vol. 45, pp. 330–35.
13. E.A. Lass, M.R. Stoudt, M.E. Williams, M.B. Katz, L.E. Levine, T.Q. Phan, T.H. Gnaeupel-Herold, and D.S. Ng: *Metall. Mater. Trans. A Phys. Metall. Mater. Sci.*, 2017, vol. 48, pp. 5547–58.
14. K. Kulawik, P.A.A. Buffat, A. Kruk, A.M.M. Wusatowska-Sarnek, and A. Czyrska-Filemonowicz: *Mater. Charact.*, 2015, vol. 100, pp. 74–80.
15. P.D. Enrique, Z. Jiao, N.Y. Zhou, and E. Toyserkani: *J. Mater. Process. Technol.*, 2018, vol. 258, pp. 138–43.
16. X. Tingdong: *Philos. Mag. Lett.*, 2006, vol. 86, pp. 501–10.
17. K. Banerjee: *Mater. Sci. Appl.*, 2011, vol. 02, pp. 1243–55.
18. J. Teimouri, S.R. Hosseini, and K. Farmanesh: *Metallogr. Microstruct. Anal.*, 2018, vol. 7, pp. 268–76.
19. X. Liu, J. Dong, X. Xie, and K.-M. Chang: *Mater. Sci. Eng. A*, 2001, vol. 303, pp. 262–66.
20. M. Anderson, A.L. Thielin, F. Bridier, P. Bocher, and J. Savoie: *Mater. Sci. Eng. A*, 2017, vol. 679, pp. 48–55.
21. G.F.V. Voort, J.W. Bowman, and R.B. Frank: *Miner. Met. Mater. Socitety*, 1994, pp. 489–98.
22. L.M. Suave, D. Bertheau, J. Cormier, P. Villechaise, A. Soula, Z. Hervier, and J. Laigo: *MATEC Web Conf.*, 2014, vol. 14, p. 21001.
23. A. Chamanfar, L. Sarrat, M. Jahazi, M. Asadi, A. Weck, and A.K. Koul: *Mater. Des.*, 2013, vol. 52, pp. 791–800.
24. Y. Ruan, A. Mohajerani, and M. Dao: *Sci. Rep.*, 2016, vol. 6, pp. 1–11.
25. M.J. Donachie and S.J. Donachie: *Superalloys: A Technical Guide*, ASM International, 2002.
26. R. Vincent: *Acta Metall.*, 1985, vol. 33, pp. 1205–16.
27. T. Chen, H. John, J. Xu, Q. Lu, J. Hawk, and X. Liu: *Corros. Sci.*, 2013, vol. 77, pp. 230–45.
28. X. Li, J. Xie, and Y. Zhou: *J. Mater. Sci.*, 2005, vol. 40, pp. 3437–43.
29. X. Cao, B. Rivaux, M. Jahazi, J. Cuddy, and A. Birur: *J. Mater. Sci.*, 2009, vol. 44, pp. 4557–71.
30. S. Kou: *Welding Metallurgy, Second Edition*, John Wiley & Sons, Inc., Hoboken, 2003.
31. C.A. Huang, T.H. Wang, C.H. Lee, and W.C. Han: *Mater. Sci. Eng. A*, 2005, vol. 398, pp. 275–81.

32. M. Sundararaman and P.J. Potdar: *Superalloys 718, 625, 706 Var. Deriv.*, 2005, pp. 477–86.
33. Y.-N. Zhang, X. Cao, P. Wanjara, and M. Medraj: *J. Mater. Res.*, 2014, vol. 29, pp. 2006–20.
34. C. Yeni and M. Koçak: *Fatigue Fract. Eng. Mater. Struct.*, 2006, vol. 29, pp. 546–57.
35. R. Cortés, E.R.R. Barragán, V.H.H. López, R.R.R. Ambriz, and D. Jaramillo: *Int. J. Adv. Manuf. Technol.*, 2017, vol. 94, pp. 3949–61.
36. P.D. Enrique, Z. Jiao, N.Y. Zhou, and E. Toyserkani: *Mater. Sci. Eng. A*, 2018, vol. 729, pp. 268–75.
37. J.J.S. Dilip and G.D. Janaki Ram: *Metall. Mater. Trans. B Process Metall. Mater. Process. Sci.*, 2014, vol. 45, pp. 182–92.